Electronic Supplementary Material (ESI) for Nanoscale.

Electronic Supplementary Information

Stretchable electronic skin based on silver nanowire composite fiber electrodes for simultaneous sensing of pressure, proximity, and multidirectional strain

Yin Cheng, Ranran Wang, Haitao Zhai, and Jing Sun**

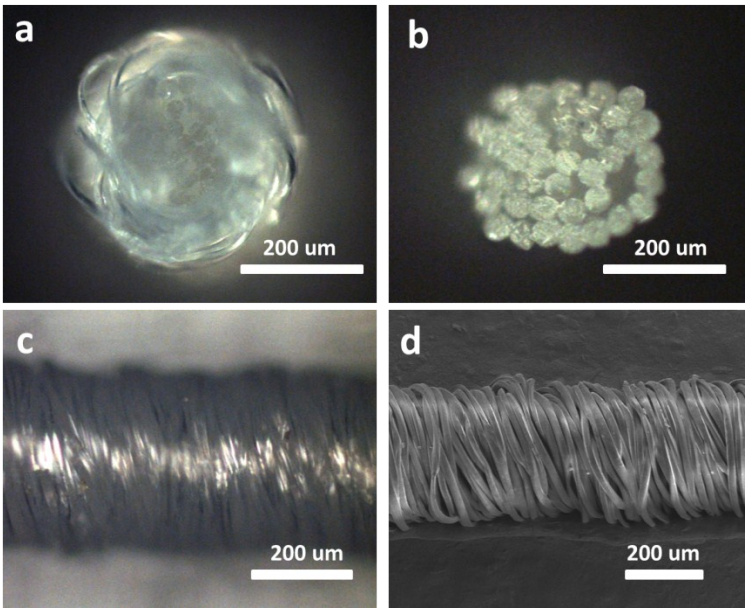

Figure S1. Structural characterization of the SCY. (a) Optical images of the cross section of the SCY (diameter of 350 um). (b) Optical image of the cross section of PU fiber (SCY without the PE yarn layer). (c) Optical image of the side view of SCY. (d) SEM image of the SCY. The PE yarn twined around the PU fiber in a right-handed pattern.

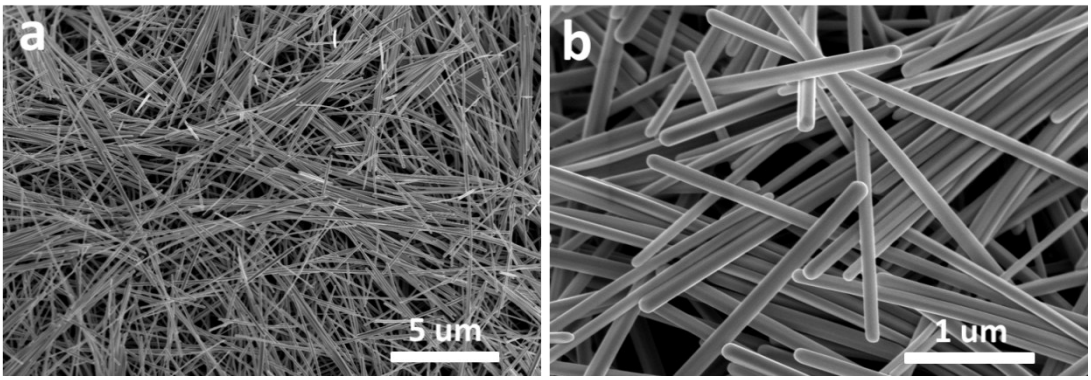

Figure S2. SEM characterization of the AgNW. SEM image of the AgNW in low (a) and high (b) magnification. The average length and diameter of the AgNW are 20 um and 120 nm, respectively.

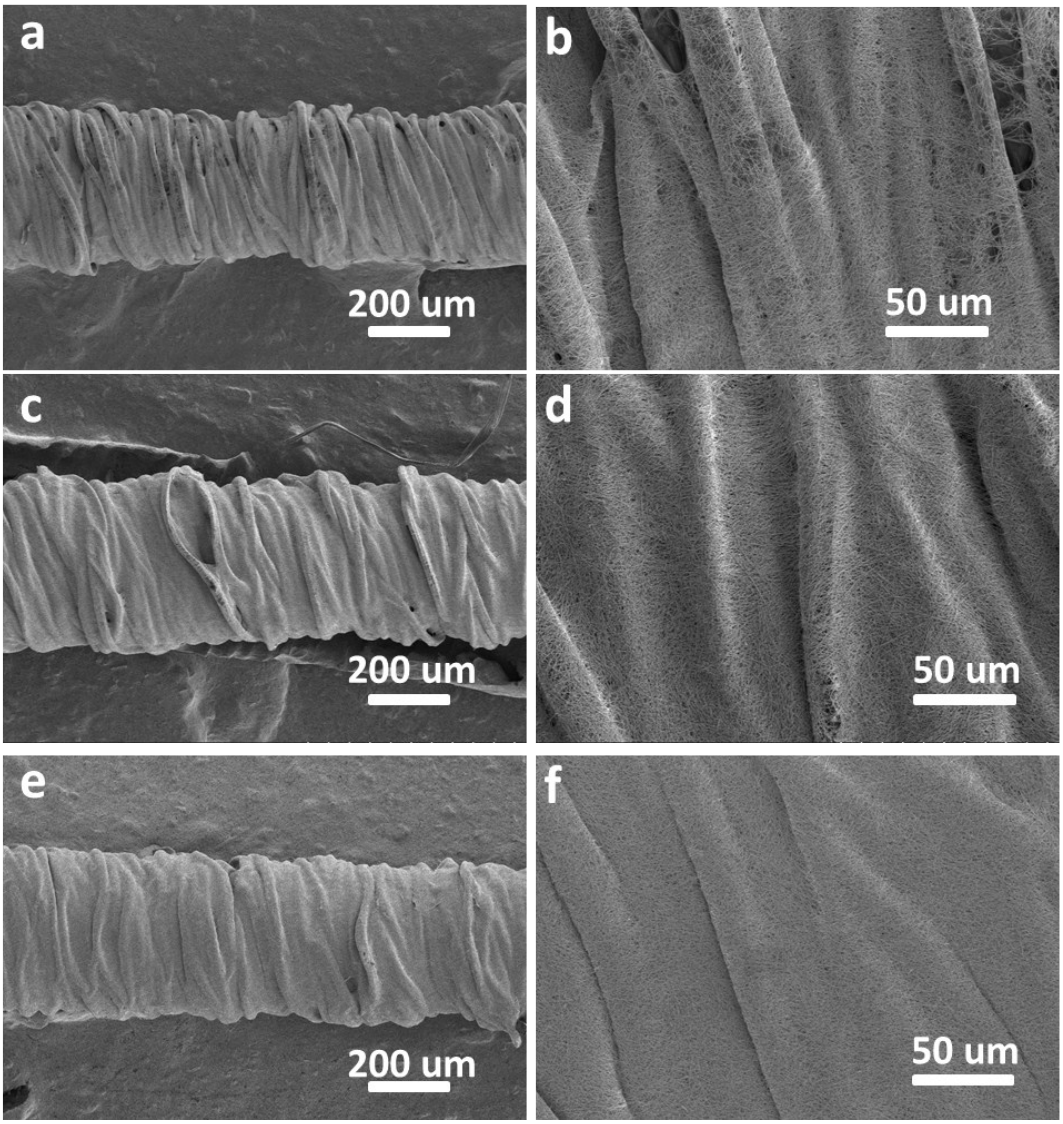

Figure S3. The SEM characterization of the fiber electrodes before pre-cracking. Low magnification SEM images of the fiber electrodes with dip-coating times of 1 (a), 3 (c), and 5 (e). High magnification SEM images of the AgNW film on the surface of SCY with dip-coating times of 1 (b), 3 (d), and 5 (f). The AgNW film coated onto the surface of the PE yarn conformably to form a blanket-like wavy configuration.

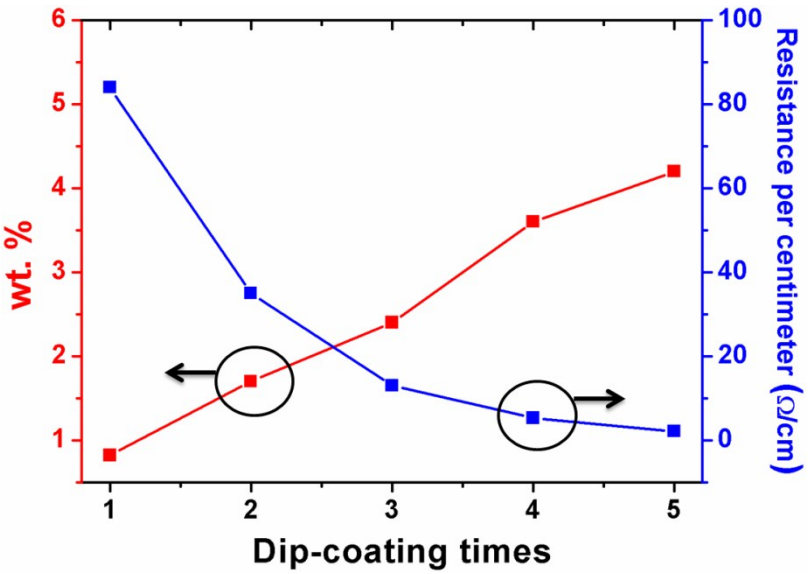

Figure S4. The tuning of the weight percentage of AgNW and conductivity (for simplicity, defined as the resistance of the fiber electrode per centimeter) of the fiber electrode before pre-cracking. With the increase of dip-coating times from 1 to 5, the weight percentage of AgNW increased from 0.82% to 4.2% almost linearly, and the resistance of the fiber electrode decreased from 84 to 2.1 Ω/cm.

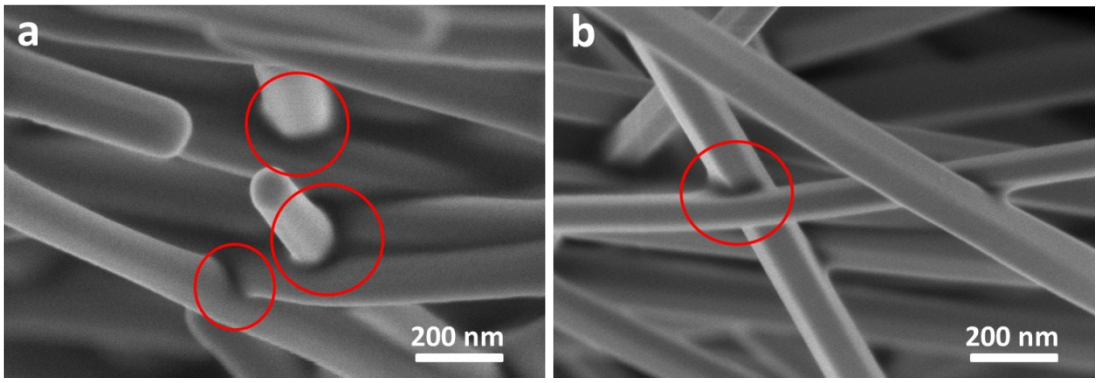

Figure S5. The nanowelding effect of the AgNW network. The annealing treatment assisted the nanowelding at the junctions of AgNW network. The red circles marked the nanowelding positons in SEM images (a) and (b).

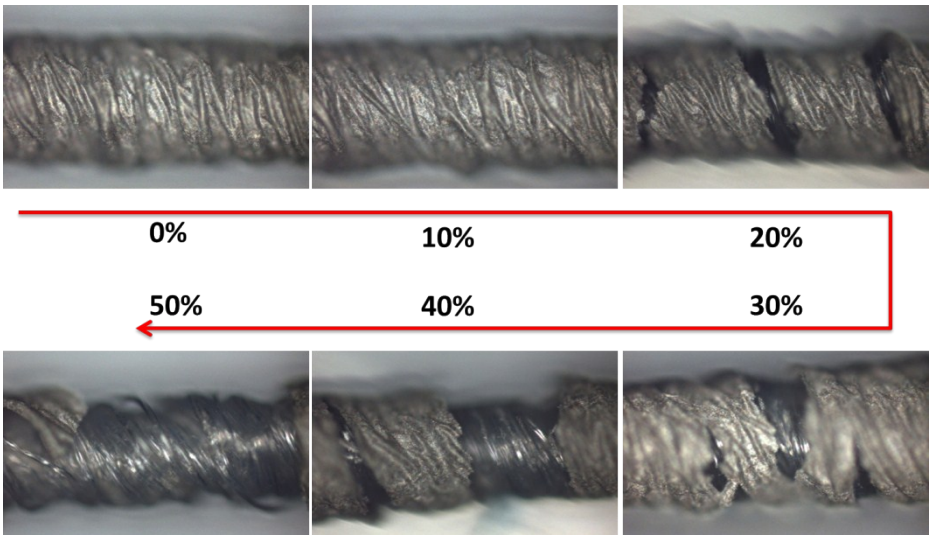

Figure S6. The microstructure variation of the fiber electrode during the first stretching up to strain of 50%. No cracks appeared within the strain range of 10%, and cracks started to be generated as the stretching went on. The crack density also increased with the strain increase. At strain of 50%, the AgNW film was already severely damaged.

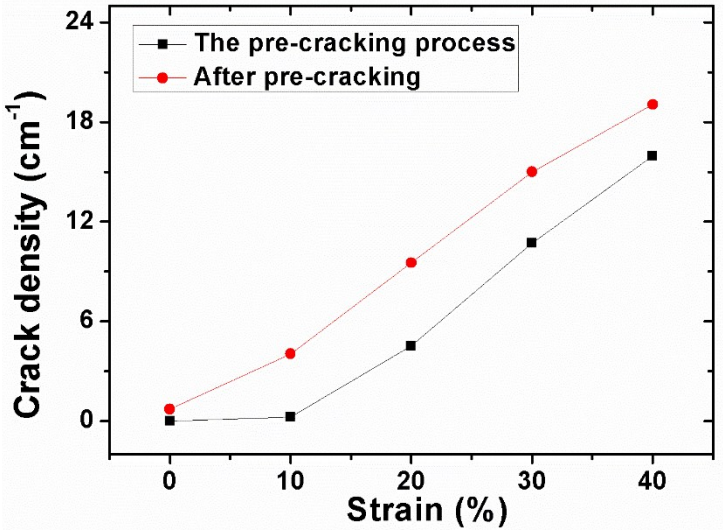

Figure S7. The crack density during the pre-cracking process and after the pre-cracking process. The crack density appeared on the surface of the fiber electrode was counted at specific strains along to 40%.

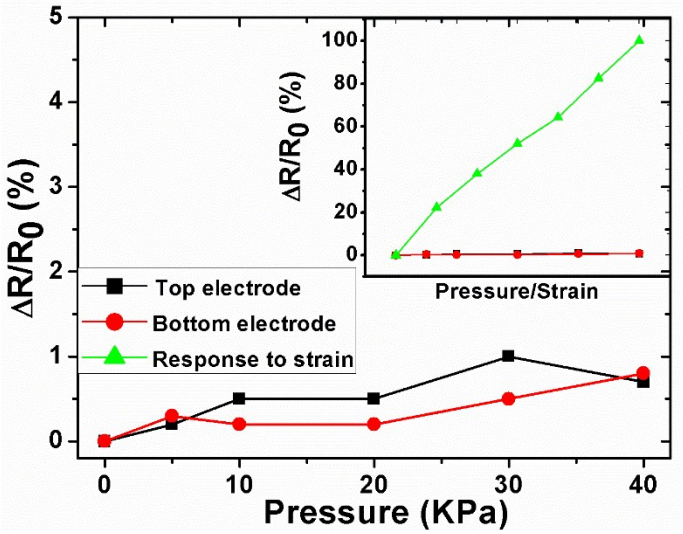

Figure S8. The influence of pressure on the resistance variation of the fiber electrode of the E-skin. Pressure up to 40 KPa was applied on the center of a sensing pixel on the E-skin and the resistance variation of the top and bottom electrodes were recorded. The inset showed the dependence of resistance variation on both the pressure (0~40 KPa) and strain (0~30%) as comparison. Clearly, compared with the resistance variation output signal corresponding to the strain, the output signal caused by pressure could be neglected reasonably.

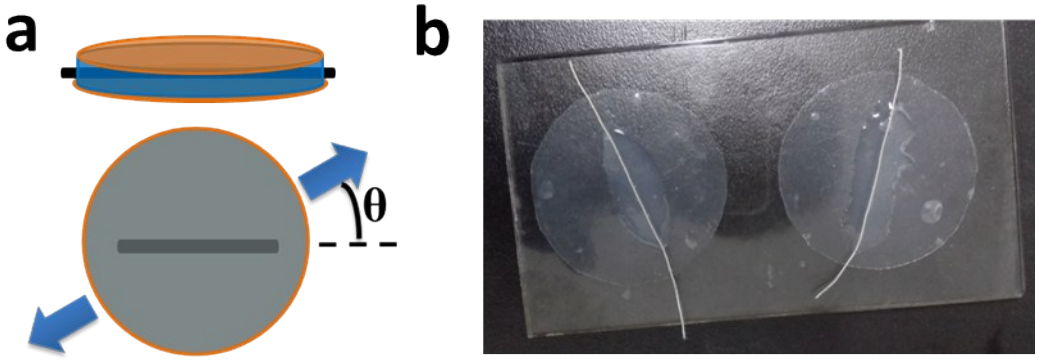

Figure S9. The disk-shaped E-layer for multidirectional strain sensing. (a) The schematic diagram of the disk-shaped E-layer. Top: side view; bottom: front view. θ denotes the angle between the stretching direction and the axial direction of the fiber electrode. (b) The photos of the disk-shaped E-layer.

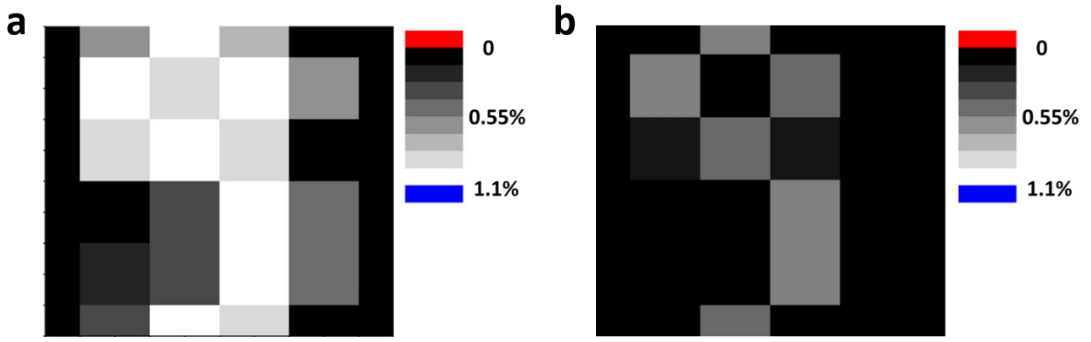

Figure S10. The pressure mapping of the rubber letter "S" on E-skin with dielectric layer of Ecoflex 00-30 (a) and Dragon-skin 10 (b). Compared with the pressure mapping of Ecoflex 00-30, the mapping with a dielectric layer of larger modulus (Dragon-skin 10) clearly exhibited weaker signal strength, and yet much higher resolution as the relatively high modulus deterred the pressure influence on the nearby sensing pixels.

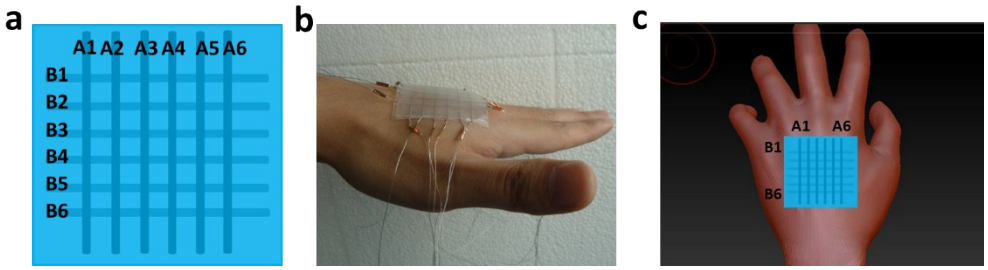

Figure S11. E-skin attached onto back of human hand to monitor bending motions. (a) The front view of schematic of the E-skin and the numbering of the fiber electrodes. (b) The photo of the E-skin attached onto the back of human hand. (c) The schematic of the E-skin attached onto the back of human hand and the numbering of the fiber electrodes.

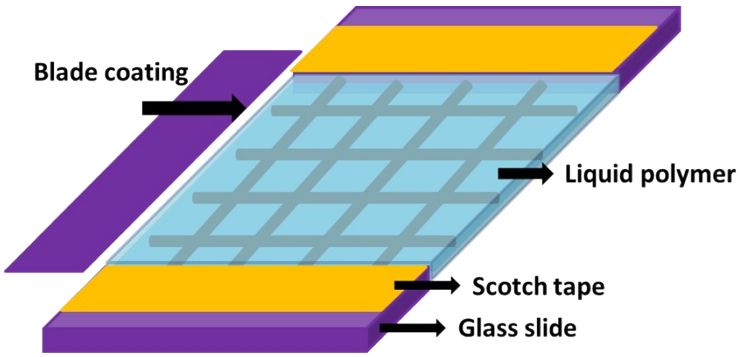

Figure S12. Schematic diagram of the blading assisted method to improve the homogeneity of the thickness distribution. We adopted a blading assisted method to further smooth the surface after the liquid polymer was coated. For example, in the fabrication of S-layer, liquid PDMS was first poured on to a Si wafer and then spin-coated. However, the relatively high viscosity made it hard to form a homogeneous thickness distribution. Then, the substrate was put in between two glass slides, with scotch tapes stuck on the surface of the glass slides. Another glass slide was used as a blade to stick close to the scotch tape and scrape across the S-layer, to obtain an evenly distributed liquid thickness. The thickness could be well tuned through the number of scotch tape layers.

Table S1. The materials choice of each layer of three different E-skin samples.

Samples of E-skin	S-layer	E-layer	D-layer
1 (PDMS)	PDMS	Ecoflex 00-30	Ecoflex 00-30
2 (Dragon skin)	PDMS	Dragon skin 10	Dragon skin 10
3 (Ecoflex)	PDMS	PDMS	PDMS

Pressure sensing mechanism analysis

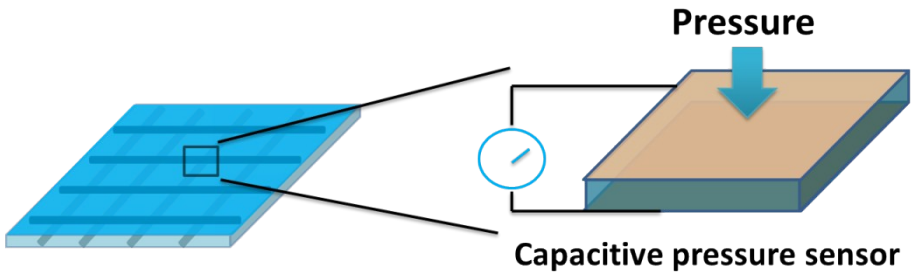

Schematic illustration of the sensing pixel simplified as parallel plate capacitor

To investigate the pressure sensing mechanism of the E-skin, we focused on a sensing pixel and simplified it as a parallel plate capacitor, as seen in the schematic illustration above. Then the capacitance C of the sensing pixel was:

$$C = \varepsilon \cdot \frac{S}{d} \quad (1)$$

Here ε is the permittivity of the D-layer, S is the electrode area, and d is the thickness of the D-layer, i.e. the distance between the two electrodes.

During the pressing, we assumed the electrode area variation could be neglected compared with the variation of thickness of the D-layer, then the relative capacitance variation was:

$$\frac{\Delta C}{C_0} = \frac{C - C_0}{C_0} = \frac{d_0}{d} - 1 \quad (2)$$

Here ΔC denotes the incremental capacitance, C_0 denotes the original capacitance value, and d_0 denotes the original thickness of the D-layer.

When the E-skin was pressed at the sensing pixel, supposed that the compressive strain was δ. Then we could know:

$$\delta = \frac{P}{E} \quad (3)$$

$$d = d_0 \cdot (1 - \delta) \quad (4)$$

Here P represents the pressure applied, E represents the elastic modulus of compression of the D-layer.

From equations (1)-(4), we could get:

$$\frac{\Delta C}{C_0} = \frac{P}{E - P} \quad (5)$$

To analyze the influence of E on the relative capacitance variation $\frac{\Delta C}{C_0}$, we assumed three E-skin samples with different D-layers, the elastic modulus being 0.1, 1, and 10 MPa, respectively, and plotted the curves in equation (5) by means of graphing calculator, as seen in the diagram below.

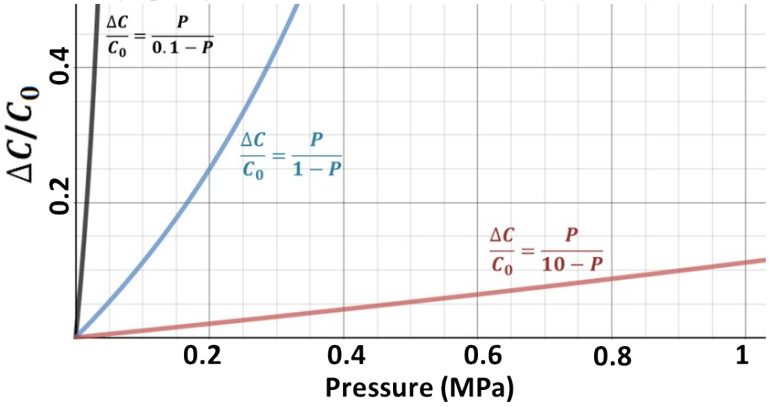

Relative capacitance variation versus the applied pressure curves of three E-skin samples

From the graphing calculating results, we could clearly draw a conclusion that the sensitivity of pressure sensing through capacitive mode depends closely on the value of E, and the smaller the value of E, the higher the pressure sensing sensitivity. To further know the changing trends of the pressure sensing curves, we further took the derivative respect to the pressure P, to obtain:

$$\frac{d\frac{\Delta C}{C_0}}{dP} = \frac{E}{(E - P)^2} \quad (6)$$

Due to the incompressibility associated with the rubber dielectric layer, P was supposed to always less than the actual E value. Under this condition, we could infer that, based on equation (6), the sensitivity of pressure sensing should increase along with the increase of pressure P, if the elastic modulus was taken as a constant parameter. However, this conclusion contradicted with the experimental results for our E-skin and also other reported papers[1-4], in which there existed a transition section between two quasi-linear sections in the $\frac{\Delta C}{C_0} \sim P$ curves. We attributed this transition to the compressive strain hardening effect of rubber materials[5, 6]. Specifically, when the pressure applied on rubbers approached a critical value, the actual elastic modulus of compression increased sharply, which would lead to a rapid decrease of the sensitivity of pressure sensing, based on equation (6). In this way, we could conclude that, typically, the high sensitivity range mainly depended on the compressive strain hardening point, after which the sensitivity went through a fast decline.

Proximity sensing mechanism analysis

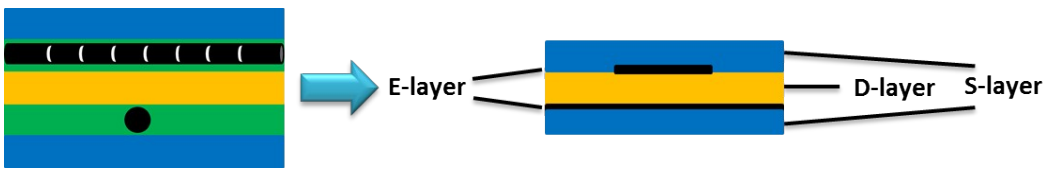

The sensing pixel simplified as a parallel plate capacitor

The sensing pixel in the E-skin could be considered as a parallel plate capacitor, as seen in the schematic illustration above, wherein the E-layers were simplified as plate electrodes. The total sensor capacitance

comprised C_p, C_{f1}, and C_{f2}, corresponding to the plate electrodes capacitance, the fringing capacitance in the D-layer (Ecoflex 00-30) and S-layer (PDMS), and the fringing capacitance through the medium directly above the sensor in the air, as seen in the schematic below. When human finger approached the sensing pixel from above, the fringing electric field in the medium of air was intercepted and shunted to directly to the ground by the finger[2, 4]. In this way, the capacitance of the sensor decreased when the human finger approached, and dropped to the lowest value when it just touched the E-skin.

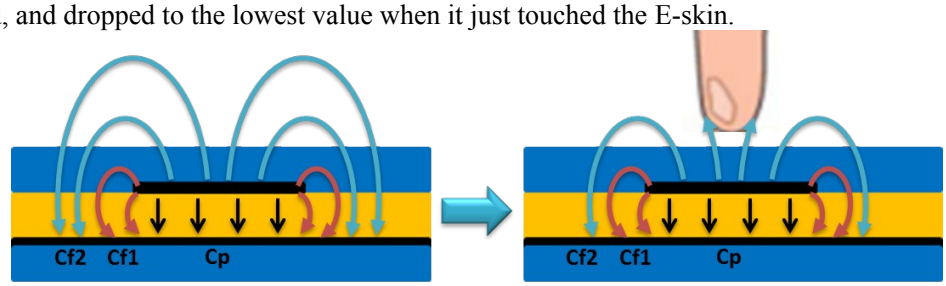

The schematic of the capacitance variation when human finger approached

Multidirectional strain sensing mechanism analysis

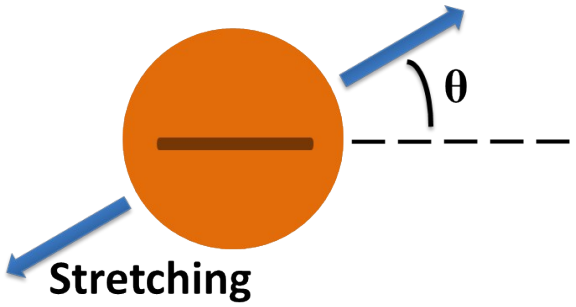

The schematic of the disk-shaped E-layer stretched in the direction of θ

To investigate the multidirectional strain sensing performance, a disk-shaped E-layer was fabricated and the lateral strain was applied in the direction of θ, which denoted the angle between the strain direction and the axial direction of the fiber electrode, as seen in the schematic above. The relative resistance variations were recorded along with the strain applied for different θ values, varying from 0 to 90 degree. The results in Figure 3f showed that, at lateral strain directions of 0, 30, 45, 60, and 90 degree, the strain sensing gauge factor were 3.2, 1.8, 0.9, 0.3 and 0. Clearly, the resistance of the fiber electrode was insensitive to the strain perpendicular to the axial direction of the fiber electrode, which we believed was because the strain perpendicular to the fiber electrode hardly caused crack generation in the surface of the fiber electrode. Only the strain component along the axial direction of the fiber electrode could effectively contribute to crack density change. Considering this, for a randomly applied strain (the maximum principal strain) in the direction of θ, we should calculate the strain component in the axial direction of the fiber electrode to predict the resistance variation. Based on plane strain transformation principles, the strain in the axial direction of fiber electrode was:

$$\varepsilon_{x^*} = \varepsilon_x \cdot (\cos 2\theta - v \sin 2\theta) \quad (7)$$

Here ε_{x^*} was the strain in the axial fiber electrode direction, ε_x denoted randomly applied strain (the maximum principal strain), θ was the applied strain direction (also the coordinate rotation angle), v was the Poisson's ratio of the disk-shaped E-layer. Similarly, the strain component in the perpendicular direction to the specified fiber electrode (denoted as ε_{y^*}, just the axial direction of the other orthogonally aligned fiber electrode) was:

$$\varepsilon_{y^*} = \varepsilon_x \cdot (\sin 2\theta - v \cos 2\theta) \quad (8)$$

From equation (7), we could know that the effective strain component along the fiber electrode decreased with the increase of θ. This prediction agreed well with the experimental results in our work.

Furthermore, as resistance variation signal of the two orthogonally aligned fiber electrodes in a sensing

pixel depended on different equations (7) and (8), through calibration, the direction and amplitude of this maximum principal strain can be determined easily by analyzing the amplitude ratio (which equals the linear strain sensing gauge factor ratio) of the two orthogonally aligned fiber electrodes' output signal. As seen in the Table S2 below, the gauge factor ratio (the same as the output signal of the two orthogonally aligned fiber electrodes under the same strain) of the two fiber electrodes in y^* and x^* directions in a sensing pixel were calculated to correspond to the strain direction θ. Once the strain direction θ was known, we could obtain the gauge factor for both of the two fiber electrodes in y^* and x^* directions from the data based on Figure 3f, and thus the amplitude of the applied strain could be calculated.

Table S2. The relation between the gauge factor (GF) ratio and the stretching direction θ

GF ratio (y/x)	**0**	**0.165**	**1**	**6.06**	**+∞**
Θ (degree)	0	30	45	60	90

References

1. S. C. Mannsfeld, B. C. Tee, R. M. Stoltenberg, C. V. Chen, S. Barman, B. V. Muir, A. N. Sokolov, C. Reese and Z. Bao, *Nat Mater*, 2010, **9**, 859-864.
2. S. Yao and Y. Zhu, *Nanoscale*, 2014, **6**, 2345-2352.
3. J. Wang, J. Jiu, M. Nogi, T. Sugahara, S. Nagao, H. Koga, P. He and K. Suganuma, *Nanoscale*, 2015, **7**, 2926-2932.
4. S. Y. Kim, S. Park, H. W. Park, D. H. Park, Y. Jeong and D. H. Kim, *Adv Mater*, 2015, **27**, 4178-4185.
5. I. D. Johnston, D. K. McCluskey, C. K. L. Tan and M. C. Tracey, *J Micromech Microeng*, 2014, **24**, 035017.
6. Hu W, Huang X, Zhang F, et al. Compressive responses of vulcanized rubber under quasi-static and high strain rate conditions. Proceedings of ICEM15, 15th International Conference on Experimental Mechanics, Porto, Portugal. 2012: 22-27.